

Crystal and electronic structure of BiTeI, AuTeI, and PdTeI compounds: A dispersion-corrected density-functional study

Sümeýra Güler-Kılıç* and Çetin Kılıç†

Department of Physics, Gebze Technical University, Gebze, Kocaeli 41400, Turkey

Published version available at <http://dx.doi.org/10.1103/PhysRevB.91.245204>

Semilocal and dispersion-corrected density-functional calculations have been performed to study the crystal structure, equation of state, and electronic structure of metal tellurohalides with chemical formula MeTeI where Me=Bi, Au, or Pd. A comparative investigation of the results of these calculations is conducted, which reveals the role of van der Waals attraction. It is shown that the prediction of crystal structure of metal tellurohalides is systematically improved thanks to the inclusion of van der Waals dispersion. It is found for BiTeI and AuTeI that the energy versus volume curve is anomalously flat in the vicinity of equilibrium volume and the calculated equation of state has an excessively steep slope in the low-pressure region, which are also fixed in the dispersion-corrected calculations. Analysis based on the computation of the volume and axial compressibilities shows that predicting the anisotropy of BiTeI via the semilocal calculations yields an *unrealistic* result whereas the results of dispersion-corrected calculations agree with the experimental compressibility data. Our calculations render that BiTeI (AuTeI) is a narrow band gap semiconductor with Rashba-type spin-splitting at the band edges (with an indirect band gap) while PdTeI is a metal with relatively low density of states at the Fermi level. The band gaps of BiTeI and AuTeI obtained via semilocal (dispersion-corrected) calculations are found to be *greater (smaller)* than the respective experimental values, which is against (in line with) the expected trend. Similarly, the Rashba parameters of BiTeI are *bracketed* by the respective values obtained via semilocal and dispersion-corrected calculations, e.g., a larger value for the Rashba parameter α_R is obtained in association with the reduction of the band gap caused by modification of the crystal structure owing to van der Waals attraction. Excellent agreement with the experimental Rashba parameters is obtained via interpolation of the calculated (semilocal and dispersion-corrected) values.

PACS numbers: 71.20.Ps, 71.70.Ej, 64.30.Jk, 31.70.-f

I. INTRODUCTION

Bismuth tellurohalide (BiTeI) has recently been attracting a great deal of interest as a potential spintronic material due to emergence of giant Rashba-type spin-splittings in its band structure¹ and of a pressure-induced topological insulating phase,^{2,3} albeit it has also been pointed out⁴ that the latter would probably be hindered by a structural phase transition. Prompted by the discovery¹ of Rashba splittings in the band structure of BiTeI, density-functional calculations have increasingly been employed⁵⁻¹⁴ to explore the electronic and crystal structure of this semiconductor. Curiously, although BiTeI is often described to have a layered structure where the triple Bi-Te-I layers are stacked along an axis perpendicular to the layers, the van der Waals attractions were *not* explicitly included in these studies. The lattice parameters of BiTeI were therefore needed to be fixed to their experimental values¹⁵ in most density-functional calculations. In order to provide a more complete description, we adopt here the dispersion-corrected density-functional (DFT-D2) approach,¹⁶ where the van der Waals forces are incorporated by means of a semiempirical force field. We employ the DFT-D2 calculations for not only BiTeI but also AuTeI and PdTeI as far as we are aware of few experimental studies¹⁷⁻¹⁹ on the structure and properties of the latter, which have not been explored via first-principles methods before.

In order to reveal the effect of the dispersion correction on the crystal and electronic structure of MeTeI (Me=Bi, Au, or Pd) compounds, we carried out our calculations at two levels of approximations: the density-functional calculations performed within the generalized gradient approximation (GGA) using the functional of Perdew, Burke, and Ernzerhof (PBE)²⁰ without and with the semiempirical dispersion correction. Hence, we compare the results of the PBE (semilocal) and PBE-D2 (dispersion-corrected) calculations to each other and to the experimental data. The total energy calculations performed for compressed and dilated systems are used to derive equation of state for metal tellurohalides under consideration. Our results show that inclusion of van der Waals interactions is necessary for an adequate physical description of these compounds. In particular, predicting the anisotropy of BiTeI via the PBE calculations yields an *unrealistic* result whereas the results of the PBE-D2 calculations agree with the experimental compressibility data.

Although oxidation state of Bi, Au, and Pd atoms is the same (+3) in the BiTeI, AuTeI, and PdTeI compounds, the crystal structures of the latter are quite different as shown in Figs. 1(a)-(c). BiTeI, AuTeI, and PdTeI crystallize in trigonal, monoclinic, and tetragonal structures with space groups $P3m1$ (No. 156), $P2_1/c$ (No. 14), and $P4_2/mmc$ (No. 131), respectively. The crystal structure of BiTeI could be characterized by the

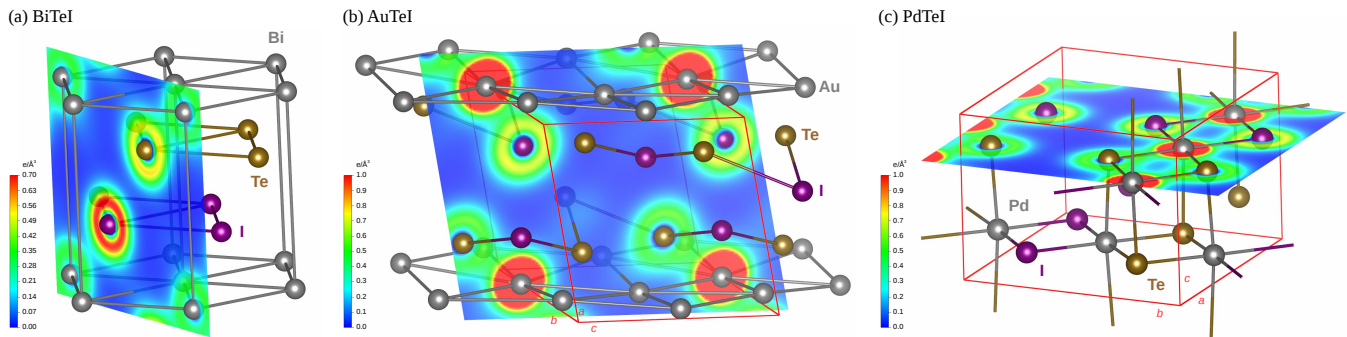


FIG. 1. (Color online) The crystal structures of BiTeI (a), AuTeI (b), and PdTeI (c) compounds. A color contour plot of the computed electronic charge density is also shown for each compound.

hexagonal lattice parameters a and c , and two internal parameters since Bi, Te, and I atoms occupy the $1a$, $1c$, and $1b$ positions with fractional coordinates $(0,0,0)$, $(2/3,1/3,z_{\text{Te}})$, and $(1/3,2/3,z_{\text{I}})$, respectively, cf. Ref. 15. As shown in Figure 1(a), adjacent trigonal layers formed by Bi, Te, and I atoms stack along the c -axis of the hexagonal lattice in BiTeI. The crystal structure of AuTeI could be characterized by the monoclinic lattice parameters a , b , c , and β , and nine internal parameters since Au, Te, and I atoms occupy the $4e$ positions with fractional coordinates $(x_{\text{Au}}, y_{\text{Au}}, z_{\text{Au}})$, $(x_{\text{Te}}, y_{\text{Te}}, z_{\text{Te}})$, $(x_{\text{I}}, y_{\text{I}}, z_{\text{I}})$, respectively, cf. Ref. 18. As shown in Fig. 1(b), the atoms form corrugated layers parallel to the bc -plane, which stack along the a -axis in AuTeI. The crystal structure of PdTeI could be characterized by the tetragonal lattice parameters a and c , and three internal parameters since Pd, Te, and I atoms occupy the $4m$, $4l$, and $4j$ positions with fractional coordinates $(0, y_{\text{Pd}}, 0)$, $(x_{\text{Te}}, 0, 0)$, and $(x_{\text{I}}, 1/2, 0)$, respectively, cf. Ref. 19. As shown in Fig. 1(c), ladder chains made of Te_2PdI_2 units running along the a - and b -axes stack along the c -axis in PdTeI. Note that the Te and I atoms are mixed in the layers or ladder chains of AuTeI or PdTeI, respectively, whereas the layers of BiTeI are unary, consisting of Bi, Te or I atoms. Accordingly, the space group of the BiTeI crystal is noncentrosymmetric while the crystal structures of AuTeI and PdTeI are centrosymmetric. This puts BiTeI in a unique position in terms of spintronic material properties,¹ which lacks inversion symmetry in the

crystal structure.

The rest of the paper is organized as follows: Sec. II is devoted to the method of calculation, giving also a summary of the computational details. We focus on the crystal structure, equation of state, and electronic band structure in Sec. III where we discuss the results of our semilocal (PBE) or dispersion-corrected (PBE-D2) density-functional calculations. A summary of our findings is given in Sec. IV. Lastly, the spin-orbit coupling (SOC) effects on the BiTeI band structure are described in further details in the Appendix.

II. METHOD

All calculated properties reported here were obtained via semilocal²⁰ (PBE) or dispersion-corrected¹⁶ (PBE-D2) density-functional calculations performed by employing the projector augmented-wave (PAW) method,²³ as implemented²⁴ in the Vienna *ab initio* simulation package²⁵ (VASP). The calculations for BiTeI and AuTeI were performed in the noncollinear mode^{26,27} of VASP in order to take spin-orbit coupling into account. The $4d$ and $5s$, $5s$ and $5p$, $5s$ and $5p$, $5d$ and $6s$, and $6s$ and $6p$ states are treated as valence states for palladium, tellurium, iodine, gold, and bismuth, respectively. Plane wave basis sets were used to represent the electronic states, which were determined by imposing a kinetic energy cutoff of 325 eV. The long-range dispersion corrections¹⁶ for periodic systems were treated as described in Ref. 28. The values of the dispersion coefficient C_6 and van der Waals radius R_0 used in this study are given in Table I. The global scaling factor s_6 was set to 0.75, which is the adequate value for the PBE functional.²⁸

We first carried out full optimization of the crystal structures where concurrent relaxations of the unit cell volume and shape as well as the ionic positions were performed with no symmetry constraints, until the maximum value of residual forces on atoms was reduced to be smaller than 0.01 eV/Å. Convergence criterion for the electronic self-consistency was set up to 10^{-6} eV. In these

TABLE I. Dispersion coefficients C_6 (in $\text{J nm}^6 \text{mol}^{-1}$) and van der Waals radii R_0 (in Å) employed in the present PBE-D2 calculations. These values are taken from the references given in the rightmost column.

Element	C_6	R_0	Reference
Pd	24.67	1.639	16
Te	31.74	1.892	16
I	31.50	1.892	16
Au	40.62	1.772	21
Bi	63.55	1.900	22

optimizations, we used the primitive unit cells of BiTeI, AuTeI, and PdTeI, whose Brillouin zones were sampled by $20 \times 20 \times 16$, $8 \times 8 \times 8$, and $21 \times 21 \times 29$ \mathbf{k} -point meshes, respectively, which were generated according to Monkhorst-Pack scheme.²⁹ Using the optimized crystal structures, we then carried out band-structure and (projected) density-of-states calculations. Besides, we performed geometry optimizations for the elemental solids of bismuth, gold, palladium, tellurium, and iodine, and employed the respective equilibrium energies per atom E_{Me} (Me=Bi, Au, Pd), E_{Te} and E_{I} in the computation of the formation energy ΔH_f . It should be reminded that the form of the electronic Hamiltonian used in dispersion-corrected (PBE-D2) calculations is the same as in the calculations employing the PBE functional alone. In other words, the effect of dispersion correction on the electronic structure is *indirectly* through modification of the crystal structure since the van der Waals interactions are treated as semiempirical force fields in the DFT-D2 approach.¹⁶

Secondly, we carried out constant-volume optimization of the crystal structures where the unit cell shape and the ionic positions were allowed to relax. Hence, we obtained the energy E per formula unit as a function of the volume V per formula unit, which was used to derive equation of state (EOS) at zero temperature. We found that the energy-volume curve is not accurately reproduced by a third-order Birch-Murnaghan (BM) fit that is in widespread use, which is further discussed in Section III. Thus, we performed forth- and fifth-order BM fits^{30,31} as a function of the Eulerian strain $f = [(V_0/V)^{2/3} - 1]/2$ that is defined from V and the zero-pressure volume V_0 , employing

$$E = E_0 + \sum_{k=2}^{k_{\text{max}}} C_{k-1} f^k \quad (1)$$

with $k_{\text{max}} = 4$ and 5 , respectively. Here C_k s are the fitting coefficients, and E_0 denotes the equilibrium energy (per formula unit). Note that $\Delta H_f = E_0 - (E_{\text{Me}} + E_{\text{Te}} + E_{\text{I}})$. The pressure P was computed by using

$$P = \frac{(1 + 2f)^{5/2}}{3V_0} \sum_{k=1}^{k_{\text{max}}-1} (k+1) C_k f^k. \quad (2)$$

The isothermal bulk modulus K_0 and its pressure derivatives K'_0 , K''_0 , and K'''_0 (all evaluated at V_0) were obtained via

$$\begin{aligned} K_0 &= \frac{2C_1}{9V_0}, \\ K'_0 &= \frac{C_2}{C_1} + 4, \\ K''_0 &= \frac{1}{K_0} \left(\frac{4C_3}{3C_1} - K'_0(K'_0 - 7) - \frac{143}{9} \right), \\ K'''_0 &= \frac{1}{9K_0^2} \left(\frac{20C_4}{C_1} - 12K_0(3K'_0 - 8)K''_0 \right. \\ &\quad \left. - K'_0[(3K'_0 - 16)^2 + 118] + \frac{1888}{3} \right), \end{aligned} \quad (3)$$

respectively.

The volume compressibility κ_v was obtained as the inverse of the bulk modulus, i.e., $\kappa_v = 1/K_0$. The axial (linear) compressibilities $\kappa_l = -(d \ln l / dP)_{P=0}$, with l denoting the lattice constant along one of the crystal axes, were computed by dividing $-\frac{1}{l} \left(\frac{dl}{dV} \right)_{V=V_0}$ by $\left(\frac{dP}{dV} \right)_{V=V_0}$, where the former [latter] was obtained via cubic spline interpolation of the lattice parameter l as a function of the volume V [via Eq. (2)]. The reliability of this procedure was tested by checking whether $\kappa_v = \kappa_a + \kappa_b + \kappa_c$ holds or not. The latter equality was satisfied in the cases of BiTeI and PdTeI, but not in the case of AuTeI. As discussed in Section III, the variation of the lattice parameter c with the pressure is nonmonotonic in the case of AuTeI, which results in a substantial error in estimating derivatives via spline interpolation. The linear compressibilities of AuTeI are therefore not reported.

III. RESULTS AND DISCUSSION

A. Crystal Structure

The crystal structure optimizations result in the experimentally determined ground-state structures, i.e., a noncentrosymmetric (centrosymmetric) crystal for BiTeI (AuTeI and PdTeI) that are shown in Fig. 1(a)-(c) where color contour plots of computed electronic charge density are also displayed. Inspection of the charge-density plot in Fig. 1(a) reveals that the most electron-rich (electron-poor) regions in BiTeI are around I (Bi) atoms. This reflects the fact that bismuth is less electronegative than both iodine and tellurium.³² It is also interesting to note that the electronegativity difference $\chi_{\text{Te}} - \chi_{\text{Bi}}$ is *positive* and comparatively *small* whereas $\chi_{\text{I}} - \chi_{\text{Bi}}$ is also *positive* but comparatively *large*.^{32,33} Accordingly, the electronic charge distribution around Bi-Te (Bi-I) bonds in Fig. 1(a) is rather of a covalent (ionic) character, which introduces an asymmetry between Bi-Te and Bi-I bonds. On the other hand, we have $\chi_{\text{Te}} - \chi_{\text{Me}} < 0 < \chi_{\text{I}} - \chi_{\text{Me}} < \chi_{\text{I}} - \chi_{\text{Te}}$ for both Me=Au and Pd, i.e., the differences $\chi_{\text{Te}} - \chi_{\text{Me}}$ and $\chi_{\text{I}} - \chi_{\text{Me}}$ are both relatively *small*, which are of the *opposite* sign.^{32,33} In agreement with the latter, the electronic charge distribution around *not only* Me-Te bonds and *but also* Me-I bonds in Fig. 1(b)-(c) look more like those of covalent bonds. Thus, the tellurium and iodine atoms prefer to coordinate with the metal atoms *almost equally*, and therefore tend to mix (as opposed to form unary layers) in the AuTeI and PdTeI compounds, rendering the crystal structures of the latter centrosymmetric.

A comparison of the results of the crystal structure optimizations (PBE and PBE-D2) to the experimental data is given in Tables II and S1 (Ref. 34). It is seen in Table II that the improvement due to the dispersion correction is mostly on the lattice parameters (a , b , c)

TABLE II. Calculated (PBE and PBE-D2) and measured lattice parameters of the MeTeI crystals. The experimental values are taken from Ref. 15, Ref. 18, and Ref. 19 for BiTeI, AuTeI, and PdTeI, respectively.

	PBE	PBE-D2	Exptl.
BiTeI			
a (Å)	4.4371	4.2843	4.3392
c (Å)	7.433	7.021	6.854
z_{Te}	0.7692	0.7479	0.6928
z_{I}	0.2828	0.3115	0.2510
AuTeI			
a (Å)	8.0057	7.2579	7.3130
b (Å)	7.8918	7.3654	7.6242
c (Å)	7.4208	7.3483	7.2550
β	104.81	103.95	106.26
x_{Au}	0.4589	0.4746	0.4654
y_{Au}	0.1333	0.1370	0.1395
z_{Au}	0.2308	0.2405	0.2370
x_{Te}	0.6481	0.6868	0.6720
y_{Te}	0.1433	0.1331	0.1301
z_{Te}	0.9821	0.9908	0.9910
x_{I}	0.1954	0.1626	0.1758
y_{I}	0.0659	0.1059	0.0857
z_{I}	0.3895	0.3799	0.3892
PdTeI			
a (Å)	8.095	7.806	7.821
c (Å)	5.722	5.652	5.659
y_{Pd}	0.2500	0.2495	0.2525
x_{Te}	0.2086	0.2262	0.2164
x_{I}	0.2321	0.2462	0.2435

whereas the PBE and PBE-D2 calculations yield errors of similar magnitude in the prediction of the internal parameters (x , y , z). It is thus notable that the prediction of unit cell volume and shape is substantially improved: Figure 2(a) displays a plot of the calculated (PBE and PBE-D2) versus experimental values for the equilibrium volume per formula unit. Although it is well known the unit cell volume is *overestimated* within the GGA, the error in the PBE-optimized volume is clearly greater than expected, which is 13.4, 16.7, and 8.3 % for BiTeI, AuTeI, and PdTeI, respectively. As evident from the trend of the empty symbols in Fig. 2(a) this anomalous overestimation is widespread. Since the lattice parameters (a , b , c) obtained in the PBE-D2 optimizations are *smaller* than those in the PBE-D2 optimizations, cf. Table II, the prediction of equilibrium volume is systematically improved thanks to the dispersion correction, as evident from the trend of the filled symbols in Fig. 2(a). Moreover, a comparison of the empty (PBE) and filled (PBE-D2) symbols of the same shape to each other in Fig. 2(b) shows that the errors in the prediction of b/a and c/a ratios are, at the same time, significantly reduced thanks to the dispersion correction.

As for the prediction of the internal parameters of the BiTeI crystal, it is interesting to compare our results to the results of Bahramy *et al.*⁵ (Sklyadneva *et al.*⁸) who predicted $z_{\text{Te}} = 0.7482$ and $z_{\text{I}} = 0.3076$ ($z_{\text{Te}} = 0.758$

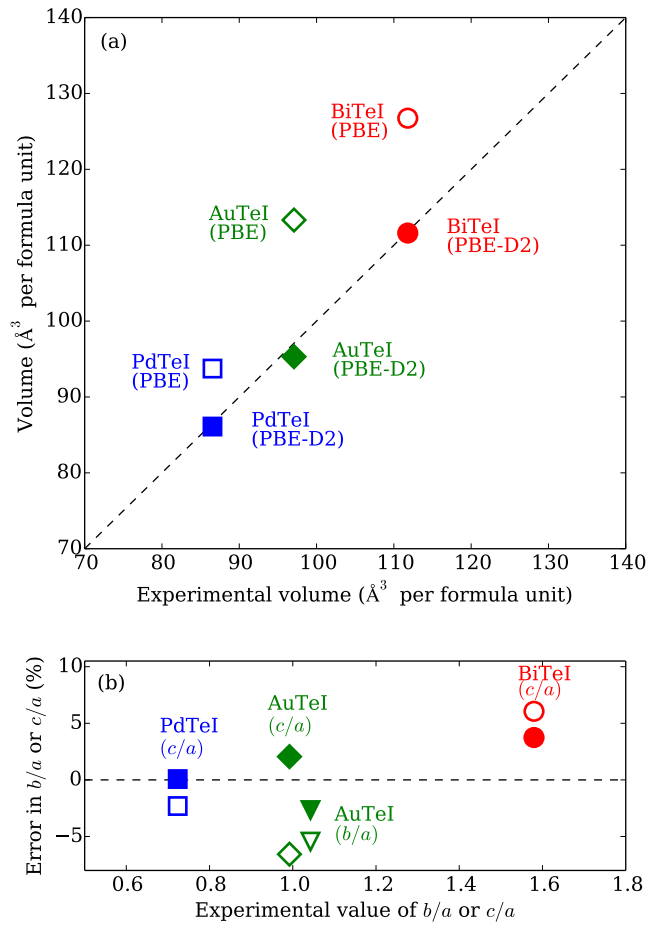


FIG. 2. (Color online) The plots of calculated versus experimental equilibrium volume (a), and error in b/a or c/a ratios (b).

and $z_{\text{I}} = 0.299$). Note that our PBE-D2 and PBE values for z_{Te} and z_{I} are in close agreement with those given by Bahramy *et al.*⁵ and Sklyadneva *et al.*,⁸ respectively -albeit in both Refs. 5 and 8 the PBE functional was employed with *no* additional terms for the dispersion correction. This is so because the lattice parameters a and c were fixed to their experimental values (that are close to our PBE-D2 values) in Ref. 5, which was not done in Ref. 8.

The predictions of Ref. 5 and 8 show that the computed values of the equilibrium Bi–Te and Bi–I distances correspond to the Bi–I and Bi–Te distances in the experimentally determined structure,¹⁵ respectively, which is supported by our PBE-D2 values, cf. Table S1 (Ref. 34). Note that in Ref. 15 the bond lengths given in Table 3 are *not* consistent with the internal parameters given Table 2. It is therefore problematic to perform a *direct* comparison of experimental and optimized values of the internal lattice parameters z_{Te} and z_{I} . Thereupon, we considered a second “phase” for BiTeI, which was generated by *exchanging* the positions of Te and I atoms so that

the Te and I atoms occupy the $1b$ and $1c$ positions with fractional coordinates $(1/3, 2/3, z_{\text{Te}})$, and $(2/3, 1/3, z_{\text{I}})$, respectively. The crystal structure optimization performed for this second phase yielded $z_{\text{Te}} = 0.2520$ and $z_{\text{I}} = 0.6884$, and the total energy *the same as* that of the BiTeI phase described in Sec. I and Table II. In line with the latter, comparison performed with the aid of the COMPSTRU program³⁵ proved that this second BiTeI phase (Te atoms residing at $1b$ positions with $z_{\text{Te}} = 0.2520$ and I atoms residing at $1b$ positions with $z_{\text{I}} = 0.6884$) is indeed *identical* to the first one (Te atoms residing at $1c$ positions with $z_{\text{Te}} = 0.7479$ and I atoms residing at $1b$ positions with $z_{\text{I}} = 0.3115$). It is interesting to point out that excellent agreement between experimental data and our computed values ($z_{\text{Te}} = 0.2520$ and $z_{\text{I}} = 0.6884$) is obtained *once* the positions of Te and I atoms are exchanged in the experimental¹⁵ crystal structure of BiTeI. As long as the x-ray diffraction fails to distinguish the Te and I layers in BiTeI,⁵ we anticipate that a full-fledged experimental characterization would render the values of z_{Te} and z_{I} in agreement with our optimized (PBE-D2) values given in Table II.

B. Equation of State

A plot of the energy difference $\Delta E = E - (E_{\text{Me}} + E_{\text{Te}} + E_{\text{I}})$ with respect to the volume V is given in Figs. 3(a), (b), and (c) for BiTeI, AuTeI, and PdTeI, respectively. The calculated values are represented by the blue (PBE) and red (PBE-D2) circles. The solid-line curves connecting the symbols show the fourth- and fifth-order BM fits, whose equation is given by $\Delta E = \Delta H_f + \sum_{k=2}^{k_{\text{max}}} C_{k-1} f^k/k$, cf. Eq. (1). Although we first performed the BM fits with $k_{\text{max}} = 3$, we found it necessary to increase k_{max} to 4 for AuTeI and PdTeI and to 5 for BiTeI in order to ensure a satisfactory level of accuracy in the fitting procedure, as mentioned in Section II. It is discernible in Fig. S1 (Ref. 34) that a good fit is not obtained when k_{max} is reduced to 4 for BiTeI, and 3 for AuTeI and PdTeI.

The values of C_k parameters obtained via fitting as well as the formation energies ΔH_f are given in Table III. Note that while ΔH_f is significantly (AuTeI) or slightly (PdTeI) reduced due to addition of the dispersion terms to the PBE functional, both PBE and dispersion-corrected (PBE-D2) calculations yield a similar degree of overbinding for BiTeI since the experimental value³⁶ of the enthalpy of formation for BiTeI is $\Delta H_f^0(298 \text{ K}) = 0.856 \text{ eV}$ per formula unit. On the other hand, the interlayer binding energy of BiTeI was computed to be 24 and 332 meV per formula unit in our PBE and PBE-D2 calculations, respectively. Thus, the dispersion-corrected (PBE-D2) calculations yield a substantially stronger interlayer binding for BiTeI, compared to the PBE calculations. It is also notable that the PBE-calculated binding curves of BiTeI [Fig. 3(a)] and AuTeI [Fig. 3(b)] are anomalously flat in the vicinity of equilib-

rium volume V_0 (and especially for volumes larger than V_0), which is not the case for PdTeI [Fig. 3(c)]. This flatness of the binding curves could be attributed to lacking van der Waals interactions because the dispersion-corrected (PBE-D2) binding curves have a significantly increased curvature.

The pressure-volume curves are shown in Figs. 3(d), (e), and (f) for BiTeI, AuTeI, and PdTeI, respectively. The graphs given in Figs. 3(g)-(m) shows the variation of the lattice parameters (a , b , c) with the pressure. The experimental compressibility data³ is also included in Figs. 3(d), (g), and (h) for comparison. The experimental data employed in Fig. 5 of Ref. 14 is not presented in Fig. 3(d) since it seems to be shifted in comparison to the data of Ref. 3, cf. Fig. S2 (Ref. 34), which also does not agree with the equilibrium volume reported in Ref. 15. It is noticeable in Fig. 3(d) that the dispersion-corrected $V(P)$ curve is in much better agreement with the experimental data (the empty circles) whereas the PBE-calculated curve has a substantially larger slope in the low-pressure region. The latter appears to be the case with AuTeI too, cf. Fig. 3(e). In contrast, the PBE-calculated and dispersion-corrected (PBE-D2) curves for PdTeI have comparable slopes even in the low-pressure region. Note that the steeper decay of $V(P)$ curve in the low-pressure region could be traced back to the variation of lattice parameters c and a for BiTeI and AuTeI, respectively, cf. Figs. 3(h) and (i). Thereupon, the error in the PBE calculations is clearly not restricted to the overestimation of the volume for quasi-layered systems, e.g., Figs. 1(a) and (b). One should, on the other hand, also notice that the agreement between the PBE-D2 and experimental curves in Fig. 3(d) is rather coincidental since the lattice parameter c (a) is overestimated (underestimated) in the PBE-D2 calculations, regardless the value of P , cf. Figs. 3(g) and (h). Furthermore, the calculated and experimental values in Fig. 3 refer to zero and room temperature, respectively. Therefore, a comparison of the relative volume (V/V_0) versus normalized pressure (P/K_0) curves is given in Fig. 4 for BiTeI, following a proposal of Ref. 37 [where using a simple *scaling* of variables was demonstrated to be practical in comparing the calculated $P(V)$ equation to the experimental equation of state]. It is seen in Fig. 4 that the experimental data points are *bracketed* by the PBE-calculated and dispersion-corrected (PBE-D2) curves, which are seemingly in better agreement with the PBE-D2 curve than the PBE curve.

Turning back to Fig. 3, it is interesting to point out that the variation of the lattice parameter c of AuTeI with the pressure is slightly increasing (nonmonotonic) according to the results of the PBE-D2 (PBE) calculations, as shown in Fig. 3(k). This implies that the lattice of AuTeI would expand along the c -axis under compression. In other words, the linear compressibility κ_c of AuTeI is *negative* according to our calculations, cf. Fig. 3(k). It should be remarked that this prediction calls for experimental verification inasmuch as the compress-

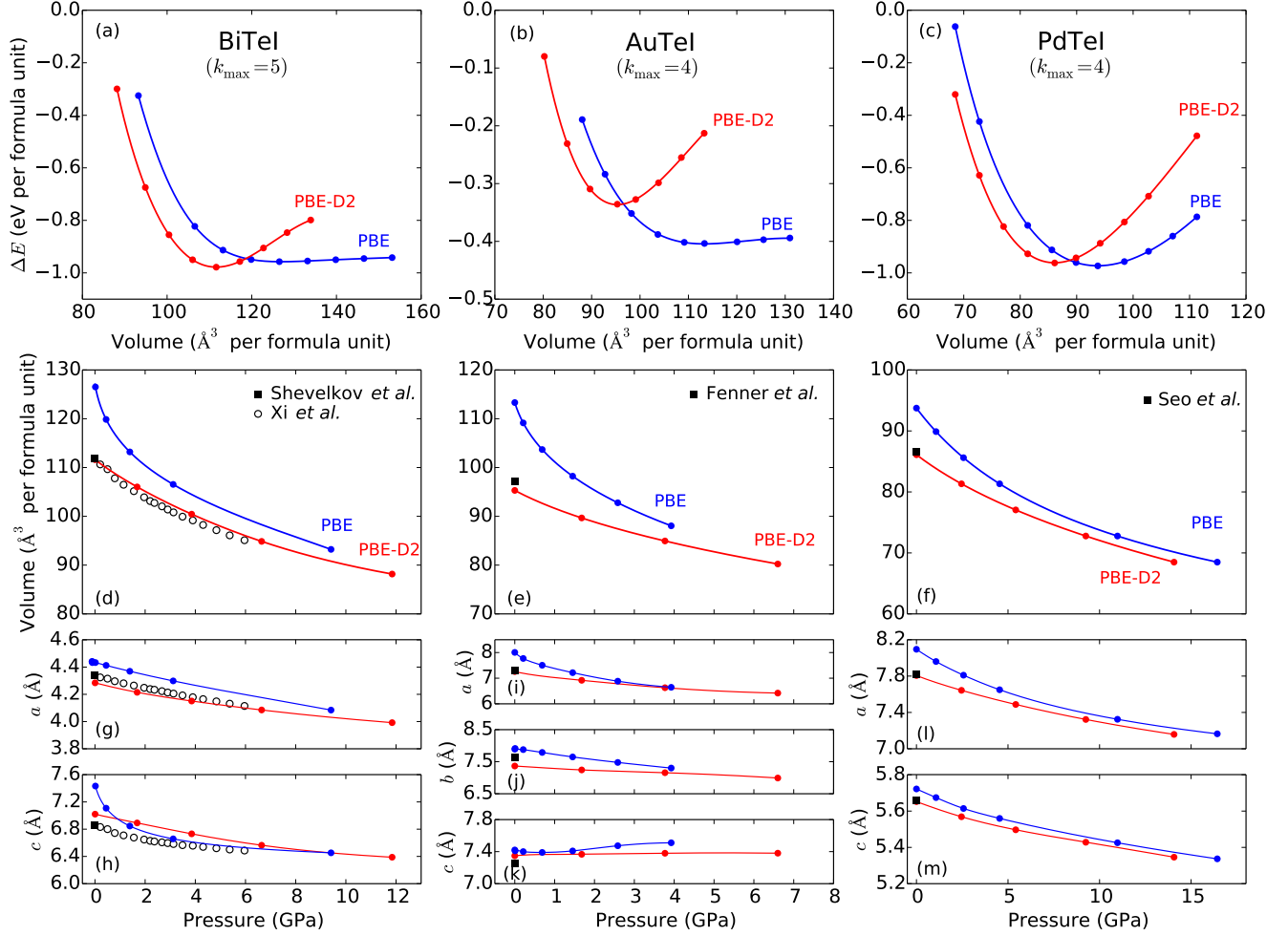


FIG. 3. (Color online) The plot of the energy difference $\Delta E = E - (E_{\text{Me}} + E_{\text{Te}} + E_{\text{I}})$, cf. Eq. (1), versus the volume for BiTeI (a), AuTeI (b), and PdTeI (c). Here k_{max} is set to 4 for BiTeI, and 3 for AuTeI and PdTeI. The respective pressure-volume curves are plotted in (d), (e), and (f). The variation of the lattice parameters (a , b , c) with the pressure is shown in (g)-(m). The PBE-calculated and dispersion-corrected (PBE-D2) curves are in blue and red, respectively. The filled symbols mark the experimental values of the equilibrium volumes [(d)-(f)] and lattice parameters [(g)-(m)] measured by Shevelkov *et al.* (Ref. 15), Fenner *et al.* (Ref. 18), and Seo *et al.* (Ref. 19) for BiTeI, AuTeI, and PdTeI, respectively. The empty circles in (d), (g), and (h) represent the experimental compressibility data of Xi *et al.* (Ref. 3) for BiTeI.

TABLE III. The values of the formation energy ΔH_f , the equilibrium volume V_0 , and the fitting coefficients C_k in Eq. (1) for MeTeI (Me=Bi,Au,Pd) compounds.

		k_{max}	ΔH_f (eV)	$V_0(\text{\AA}^3)$	C_1 (eV)	C_2 (eV)	C_3 (eV)	C_4 (eV)
BiTeI	PBE	5	-0.958	127.039	15.357	278.613	1091.512	-8932.044
	PBE-D2	5	-0.978	111.626	88.806	228.317	-4645.020	30756.053
AuTeI	PBE	4	-0.404	113.317	13.558	172.994	-444.287	
	PBE-D2	4	-0.337	95.308	58.526	244.128	-1103.027	
PdTeI	PBE	4	-0.973	93.742	61.728	-11.560	506.408	
	PBE-D2	4	-0.961	86.101	90.574	103.902	-695.661	

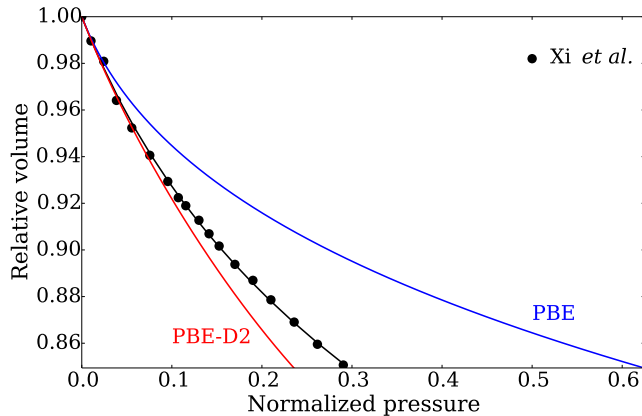


FIG. 4. (Color online) The plot of the relative volume V/V_0 versus the normalized pressure P/K_0 for BiTeI. The PBE-calculated and dispersion-corrected curves are in blue and red, respectively. The black (solid) circles represent the experimental data of Xi *et al.* (Ref. 3). The black curve was obtained by performing a third-order BM fit to the latter.

ibility of AuTeI has not been investigated before, to our knowledge. Note that the usual behavior under compression is that the individual lattice parameters decrease so that $\kappa_l > 0$, which is the case in Figs. 3(g)-(j) and (l)-(m). The behavior of *negative linear compressibility* has nevertheless been observed in a number of systems^{38–41} recently.

The bulk modulus K_0 and its pressure derivatives K'_0 , K''_0 , and K'''_0 computed via Eq. (3) with C_k coefficients listed in Table III are given in Table IV where the experimental values for BiTeI are also included. The latter were obtained by performing a third-order BM fit, cf. the black solid curve in Fig. 4, to the experimental compressibility data.³ It is seen that the PBE calculation yields a substantially underestimated (overestimated) value for K_0 (K'_0) of BiTeI. Recalling that (i) the PBE-calculated binding energy curve anomalously flat in the vicinity of equilibrium volume, cf. Fig. 3(a), and (ii) the PBE-calculated equation of state has an excessively steep slope in the low-pressure region, cf. Fig. 3(d), it is

TABLE IV. The bulk modulus K_0 (in GPa) and its pressure derivatives K'_0 , K''_0 (in GPa^{-1}), and K'''_0 (in GPa^{-2}).

		k_{\max}	K_0	K'_0	K''_0	K'''_0
BiTeI	PBE	5	4.3	22.1	-59.6	658.8
	PBE-D2	5	28.3	6.6	-2.9	2.5
	Experimental	3	20.5	7.6		
AuTeI	PBE	4	4.3	16.8	-52.4	
	PBE-D2	4	21.9	8.2	-2.3	
PdTeI	PBE	4	23.4	3.8	0.3	
	PBE-D2	4	37.5	5.1	-0.4	

TABLE V. The volume (κ_v) and axial (κ_a and κ_c) compressibilities (in GPa^{-1}), and their ratios.

	κ_v	κ_a	κ_c	κ_a/κ_v	κ_c/κ_v	κ_a/κ_c
BiTeI	PBE	0.232	0.010	0.212	0.043	0.914
	PBE-D2	0.035	0.011	0.013	0.314	0.371
PdTeI	PBE	0.043	0.017	0.008	0.395	0.186
	PBE-D2	0.027	0.010	0.007	0.370	0.259

no surprise that the bulk modulus is substantially underestimated in the PBE calculations. The PBE-calculated first pressure derivative K'_0 is consequently greatly overestimated, balancing this underestimation of K_0 . On the contrary, the dispersion-corrected (PBE-D2) calculations, albeit in much better agreement with the experimental values, result in overestimation (underestimation) for K_0 (K'_0). Hence, the experimental values of K_0 and K'_0 are *bracketed* by the PBE-calculated and dispersion-corrected (PBE-D2) values.

The volume (bulk) and axial (linear) compressibilities and their ratios are given in Table V for BiTeI and PdTeI. Note that $\kappa_b = \kappa_a$ for these systems. For BiTeI (PdTeI), the PBE and PBE-D2 values for the a -axis (c -axis) compressibility are close to each other. In contrast, $\kappa_c^{\text{PBE}} \ll \kappa_c^{\text{PBE-D2}}$ for BiTeI, and $\kappa_a^{\text{PBE}} > \kappa_a^{\text{PBE-D2}}$ for PdTeI. Thus, the c -axis compressibility of BiTeI is greatly overestimated in the PBE calculations (which reflects lacking van der Waals binding). We have furthermore $\kappa_a/\kappa_c \ll 1$ (PBE) while $\kappa_a/\kappa_c \sim 1$ (PBE-D2), and $\kappa_a/\kappa_v < 1/3$ and $\kappa_c/\kappa_v > 1/3$ (PBE) while $\kappa_a/\kappa_v \sim 1/3$ and $\kappa_c/\kappa_v \sim 1/3$ (PBE-D2) for BiTeI. Note that the ratio κ_a/κ_c should be unity, and both κ_a/κ_v and κ_c/κ_v need to be equal to $1/3$ for *isotropic* materials. For *layered* materials, on the other hand, one would expect to have the ratio κ_a/κ_v (κ_c/κ_v) significantly smaller (larger) than $1/3$ and the ratio κ_a/κ_c much smaller than unity (e.g., $\kappa_a/\kappa_v = 0.028$, $\kappa_c/\kappa_v = 0.943$, $\kappa_a/\kappa_c = 0.03$ for graphite,⁴² a most known layered material). Thus, the PBE calculations predict BiTeI to be an extremely layered material whereas the PBE-D2 calculations indicate a layered, but substantially less anisotropic material. In other words, predicting the anisotropy of BiTeI via the PBE calculations yields an *unrealistic* result, given that the PBE-D2 calculations are in much better agreement with the experimental compressibility data. It appears that the inclusion of van der Waals attraction, which was motivated by the quasi-layered structure of BiTeI, leads to a much less anisotropic crystal structure. Note that this issue does not raise in the case of PdTeI where van der Waals binding plays a much less prominent role and therefore the PBE and PBE-D2 calculations *qualitatively* yield similar results, cf. Table V.

C. Electronic Structure

Figure 5(a)-(c) displays the calculated band structure (left panels in each subplot) and projected density of states (right panels in each subplot) of the MeTeI compounds under consideration, obtained by using the optimized (PBE-D2) lattice parameters given in Table II. BiTeI and AuTeI appear to be narrow band gap semiconductors whereas PdTeI is predicted to be a metal with relatively low density of states at the Fermi level E_F . In Fig. 5(a), Rashba-type splitting near the Brillouin zone point A is visible, which is in agreement with the former studies.^{1,5} This is important because the emergence of the bulk Rashba-type splittings in the calculated band structure *depends* on the reliable prediction of the BiTeI lattice parameters, cf. Fig. 4 of Ref. 13. We present a comparison of the BiTeI band structures *with and without* SOC in the Appendix, which confirms that splitting near the point A in Fig. 5(a) manifests SOC-induced modification of the band edges. It is further shown that the gradient of the crystal potential $\vec{\nabla}V(\mathbf{r})$ leads predominantly to an asymmetric electric field along the c -axis that facilitates the spin-orbit coupling. As long as the latter gives rise to an effective magnetic field⁴³ \vec{H}_{eff} , a simple understanding is that Rashba-type splitting in Fig. 5(a) originates from the interaction of the crystal electrons with \vec{H}_{eff} that is proportional to $\vec{\nabla}V(\mathbf{r}) \times \mathbf{p}$, where \mathbf{p} denotes the momentum operator. It is to be noted that a comprehensive analysis has already been given by Bahramy *et al.* in Ref. 5, revealing the origin of (giant) Rashba-type splitting in BiTeI.

We see in Fig. 5(a) that the lower valence band consists of the Bi, Te, and I s orbitals whereas the upper valence band as well as lower conduction band are derived from the Bi, Te, and I p orbitals. Fig. 5(b) shows that the bands of AuTeI are relatively flat (nondispersive), which are derived primarily from Te and I s orbitals (lower valence band), and Te and I s and Au d orbitals (upper valence band as well as lower conduction band). Au d states dominate the bottom of the upper valence band. Fig. 5(c) shows that the bands of PdTeI around the Fermi level are quite dispersive along not only perpendicular Γ - Z direction but also parallel Γ - M and X - M directions. Thus our calculations indicate that opening a band gap owing to a possible c -axis-doubling distortion¹⁹ would probably not render PdTeI a semiconductor. We see in Fig. 5(c) that the deep-lying bands consists mainly of the Te s and I s orbitals while the bands in the vicinity of the Fermi level are derived from the Te p , I p and Pd d orbitals.

Table VI gives some characteristic band structure parameters for BiTeI and AuTeI semiconductors, for which experimental data is available: the band gap E_g and the Rashba energy E_R and momentum offset k_R for the conduction band minimum. As for the BiTeI band gap, it is interesting to point out that our PBE-D2 value is close the PBE value (0.242 eV) of Rusinov *et al.*¹⁰ who employed the experimental¹⁵ lattice parameters a and c

TABLE VI. The calculated (PBE and PBE-D2) and experimental band structure parameters of the BiTeI and AuTeI semiconductors: the band gap E_g (in eV) and the Rashba energy E_R (in eV) and momentum offset k_R (\AA^{-1}) for the conduction band minimum.

	PBE	PBE-D2	Experimental
BiTeI			
E_g	0.432	0.207	$0.38^a, 0.36^b, 0.26^c$
E_R	0.081	0.124	0.1^a
k_R	0.0529	0.0514	0.052^a
AuTeI			
E_g (indirect)	0.938	0.623	
E_g (direct)	0.938	0.803	0.9^d

^aRef. 1 ^bRef. 44 ^cRef. 45 ^dRef. 17

and PBE-optimized⁶ internal parameters z_{Te} and z_{I} in their calculations. Similarly, our PBE-D2 values for the Rashba energy and momentum offset are in close agreement with the respective PBE values reported in Ref. 10 (where $E_R = 0.122$ eV and $k_R = 0.050$ \AA^{-1}).

It is clear from the entries of Table VI that the calculations with the PBE functional yield band gaps that are *greater* than the respective experimental values, which is against the expected trend inasmuch as the band gap is known to be *underestimated* within the GGA. Contrary to this, the calculated band gaps corresponding to the PBE-D2 optimized crystal structures are *smaller* than the respective experimental values, in line with the expected trend. Hence, the experimental band gaps are *bracketed* by the respective PBE and PBE-D2 values, i.e.,

$$E_g^{\text{PBE-D2}} < E_g < E_g^{\text{PBE}}.$$

Similarly, the experimental values of E_R and k_R are also *bracketed* by the respective PBE and PBE-D2 values (cf. Table VI) since

$$E_R^{\text{PBE}} < E_R < E_R^{\text{PBE-D2}}, \\ k_R^{\text{PBE-D2}} < k_R < k_R^{\text{PBE}}.$$

We accordingly anticipate that comparative usage of the PBE and PBE-D2 calculations would be a useful strategy for predicting the band structure of layered polar semiconductors, which eliminates the need to employ the experimental lattice parameters.

As for the Rashba parameter $\alpha_R = 2E_R/k_R$ of BiTeI, which represents the strength of Rashba splitting, the PBE-calculated and dispersion-corrected (PBE-D2) values are $\alpha_R = 3.06$ and 4.82 eV \AA , respectively, bracketing the experimental value¹ of $\alpha_R = 3.85$ eV \AA . It is shown in the Appendix that ending up with a larger Rashba parameter within the dispersion-corrected (PBE-D2) description is due to the enhancement of the asymmetric electric field $\langle -\vec{\nabla}V \rangle$ along the c -axis [Fig. A2(b)].

Given that the experimental values of k_R , E_R , and α_R are bracketed by their calculated (PBE and PBE-D2) values, one might attempt to interpolate their PBE-calculated and dispersion-corrected (PBE-D2) values in

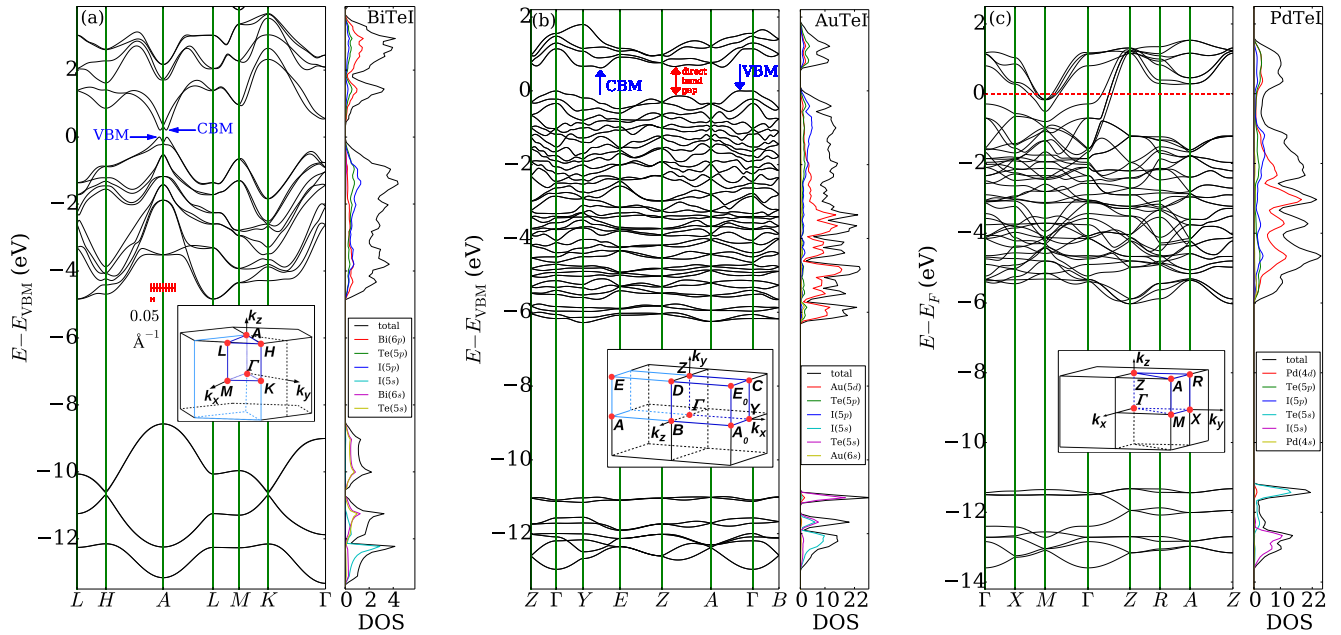


FIG. 5. (Color online) The calculated band structure (left panels in each subplots) and projected density of states (right panels in each subplots) of BiTeI (a), AuTeI (b), and PdTeI (c). The crystal structures optimized via dispersion-corrected (PBE-D2) calculations are assumed, cf. Table II.

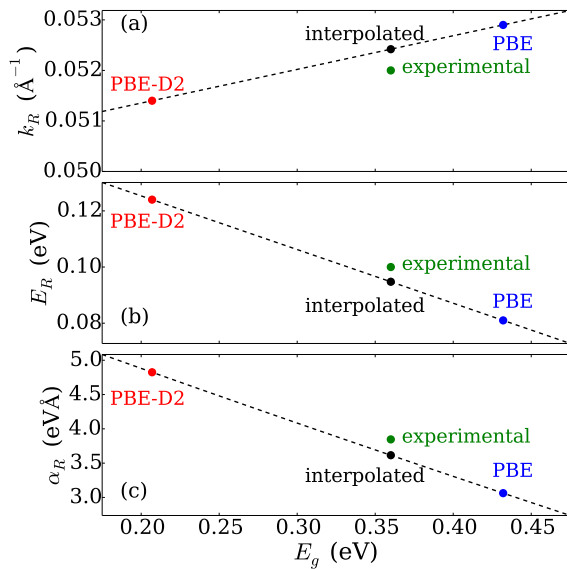


FIG. 6. (Color online) The momentum offset k_R (a), Rashba energy E_R (b), and Rashba parameter α_R (c) for the conduction band minimum of BiTeI versus the band gap E_g .

order to obtain better estimates. The band gap E_g can be used as an interpolation variable for this purpose since the values of k_R and E_R are in almost linear correlation with the band gap values, as shown in Figs. 6(a) and (b), respectively. Note that the error due to the underestimation (PBE-D2) or overestimation (PBE) of E_g could then be corrected by using the experimental value of the band

gap (i.e., $E_g = 0.36$ eV) in the interpolation. The dashed lines in Figs. 6(a) and (b) passes through the calculated points, whose equations are given by

$$\begin{aligned} k_R &= 0.05002 + 0.00667E_g, \\ E_R &= 0.16356 - 0.19111E_g, \end{aligned} \quad (4)$$

respectively. Combining the latter two equations, α_R could be obtained as a function of E_g , which is shown by the dashed line in Fig. 6(c). Substituting the experimental value of E_g in Eq. (4) yields the *interpolated* values of $k_R = 0.0524$ \AA^{-1} , $E_R = 0.095$ eV, and $\alpha_R = 3.62$ eV \AA [which are marked by the black circles in Figs. 6(a), (b) and (c), respectively] in close agreement with the respective experimental values¹ [marked by the green circles in Figs. 6(a)-(c)], cf. Table VI.

Finally, forasmuch as the pressure-induced closure of the BiTeI band gap has been explored in a number of recent studies,^{2-4,14,46,47} we estimated the critical pressure P_c at which the band gap disappears (the latter being a signature of the topological phase transition). We obtain $P_c = 3.73$ GPa using our dispersion-corrected (PBE-D2) equation of state, cf. Section III B, together with a series of band structure calculations (not shown), which confirms the refined value ($P_c = 3.5$ GPa) of Bahramy *et al.* (Refs. 2 and 46). Our investigation of the variation of the BiTeI band gap and Rashba parameters with pressure will be reported in detail in a separate publication.

IV. CONCLUSION

In summary, our comparative investigation of the results of semilocal (PBE) and dispersion-corrected (PBE-D2) calculations reveals the effect of van der Waals attractions on the crystal and electronic structure of metal tellurohalides BiTeI, AuTeI, and PdTeI. We find that the prediction of crystal structure is systematically improved thanks to the inclusion of van der Waals dispersion. It is shown for the compounds with a quasi-layered crystal structure, viz. BiTeI and AuTeI, that (i) the PBE-calculated energy versus volume curve is anomalously flat in the vicinity of equilibrium volume, and especially for volumes larger than the equilibrium volume, and (ii) the PBE-calculated equation of state has an excessively steep slope in the low-pressure region, which are also fixed in the dispersion-corrected (PBE-D2) calculations. Our analysis based on the computation of the volume and axial compressibilities shows that predicting the anisotropy of BiTeI via the semilocal calculations yields an *unrealistic* result whereas the results of the PBE-D2 calculations agree with the experimental compressibility data. Our calculations render that BiTeI and AuTeI are narrow band gap semiconductors with Rashba-type spin-splitting at the band edges and with an indirect band gap, respectively. PdTeI, on the other hand, is predicted to be a metal with relatively low density of states at the Fermi level. It is notable that the band gaps computed by using the optimized crystal structures from the PBE (PBE-D2) calculations are found to be *greater (smaller)* than the respective experimental values, which is against (in line with) the expected trend inasmuch as the band gap is known to be *underestimated* within the GGA. We also find that the Rashba parameter, Rashba energy and momentum offset of BiTeI are *bracketed* by the respective values obtained via the semilocal (PBE) and dispersion-corrected (PBE-D2) calculations. Specifically, a larger value for the Rashba parameter is obtained in the PBE-D2 calculations, which could be attributed to the reduction of the band gap caused by modification of the crystal structure owing to the inclusion of van der Waals dispersion terms. Excellent agreement with the experimental data for the Rashba parameter, Rashba energy and momentum offset of BiTeI is obtained *via* interpolation of the calculated (PBE and PBE-D2) values.

ACKNOWLEDGMENTS

We thank X. Xi and Y. Chen for providing the experimental data used in Figs. 3, 4, and S2. The drawings in Fig. 1 were produced by the visualization software VESTA.⁴⁸ The numerical calculations reported here were carried out at the High Performance and Grid Computing Center (TRUBA Resources) of TUBITAK ULAKBIM.

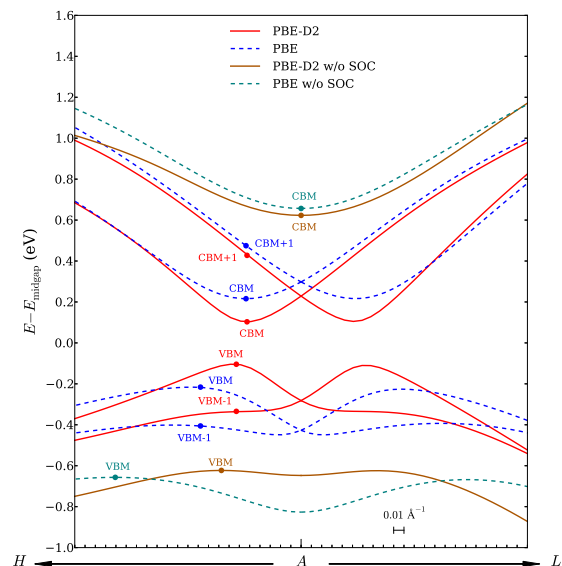


FIG. A1. (Color online) The band structure of BiTeI in the vicinity of the band edges, calculated with and without SOC and dispersion correction. The lower conduction (upper valence) band states labeled as CBM and CBM+1 (VBM and VBM-1) are marked by the solid circles.

Appendix: Spin-Orbit-Induced Modification of the BiTeI Band Edges

A comparison of the calculated band structures with and without SOC has already been presented by Bahramy *et al.* in Ref. 5 where the PBE-optimized values for z_{Te} and z_I were employed together with the *experimental* values for a and c . Here we present a similar comparison in Fig. A1 where *no* experimental data are used. The lower conduction (upper valence) band states are marked by the solid circles labeled as “CBM” and “CBM+1” (“VBM” and “VBM-1”) in Fig. A1. Table A gives the projected wave function character of these states. It is seen in Fig. A1 that Rashba-type splitting is absent in the band structures calculated *without* SOC (marked as “PBE-D2 w/o SOC” and “PBE w/o SOC”) in both cases *with and without* the dispersion correction. When SOC is taken into account, Rashba-type splitting occurs on both (conduction and valence) band edges, cf. the curves marked as “PBE-D2” and “PBE” in Fig. A1. It is thus clear that Rashba-type splitting in Fig. A1 [and Fig. 5(a)] originates from spin-orbit interaction. Thanks to the latter, the band edge states have nonvanishing contributions from p_x and p_y orbitals in comparison to the cases without SOC, which could be seen via comparative inspection of rows in Table A. Note, for example, that when SOC is ignored the character of CBM wave function ψ_c is mostly of Bi- p_z by 72% (PBE-D2) [69% (PBE)] and contribution from p_x and p_y orbitals is negligible. On the other hand, the contribution from Bi- p_z is reduced to 35% (PBE-D2) [28% (PBE)] at the expense of nonvanish-

TABLE A. The projected wave function character of the lower conduction (CBM and CBM+1) and upper valence (VBM and VBM-1) band states, cf. Fig. A1. The entry values represent, in %, the angular-momentum-resolved (s , p_x , p_y , p_z) contributions from all (Bi, Te, or I) atoms. The latter are rounded within 1%, and the contributions less than 1% are ignored.

State	Bi				Te				I			
	s	p_x	p_y	p_z	s	p_x	p_y	p_z	s	p_x	p_y	p_z
CBM+1												
PBE-D2	2	13	10	22	2	14	15	4	1			14
PBE		11	9	30	3	14	17	1	2	1		9
CBM												
PBE-D2 w/o SOC				69	12				6			11
PBE-D2		12	16	28	5	14	10		2	2	3	6
PBE		10	13	35	5	13	8		2	2	5	4
PBE w/o SOC				72	10				6			9
VBM												
PBE-D2 w/o SOC	16			1		3	9	44				24
PBE-D2	14			2		6	12	37		1	1	23
PBE	11			4		9	18	34		1	1	16
PBE w/o SOC	13			5		8	17	33		2	4	16
VBM-1												
PBE-D2	13	4	2	1		7	10	35	1	6	3	14
PBE	10	4	2			13	14	32		5	4	13

ing contributions from p_x and p_y orbitals when SOC is taken into account. Thus, as demonstrated in Fig. A2(a), the character of CBM wave function would facilitate formation of a two-dimensional electron gas *once* the Fermi level is *above* the conduction band minimum. Note that the latter is usually the case with the samples used in recent experimental studies, e.g., Refs. 1, 12, and 47. It is seen in Fig. A2 that the conduction electrons are *really* subject to an asymmetric electric field $\langle -\vec{\nabla}V \rangle$ along the c -axis [Fig. A2(b)] as mentioned in Section III C, which are to a significant extent confined in the interplanar regions (i) between Te and Bi layers as well as (ii) between the Bi and I layers [Fig. A2(a)].

Figure A2(b) also shows that the asymmetric electric field along the c -axis is substantially enhanced within the dispersion-corrected (PBE-D2) description (the red curve), compared to the PBE-calculated (blue curve). Note, for comparison, that there is an insignificant change in the ab planar average of $\vec{\nabla}V$, cf. Fig. S3 (Ref. 34). Clearly, the enhancement of the asymmetric electric field along c -axis leads to stronger SOC. Hence the value of Rashba parameter α_R obtained via the dispersion-corrected (PBE-D2) calculation turns out to be greater than the respective PBE-calculated value.

Going back to Fig. A1, it is interesting to point out that BiTeI turns out to be an indirect semiconductor in all calculations presented in Fig. A1, which is in line with the former studies.^{44,45,49} The difference $k_{\text{CBM}} - k_{\text{VBM}}$ is largest [0.181 \AA^{-1} for PBE w/o SOC] when SOC and dispersion correction are both ignored, which is reduced to 0.044 \AA^{-1} (0.077 \AA^{-1}) via inclusion of SOC (dispersion correction). Taking SOC and dispersion correction into account together yields the smallest difference $k_{\text{CBM}} - k_{\text{VBM}} = 0.010 \text{ \AA}^{-1}$ (PBE-D2). Similarly the band gap E_g is reduced from 1.313 eV (PBE w/o

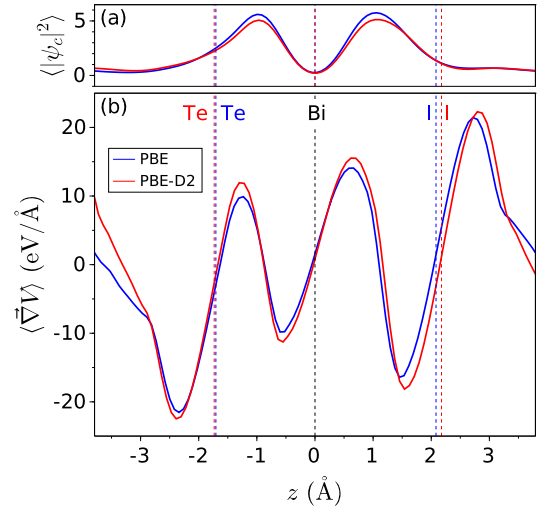


FIG. A2. (Color online) The ab planar average of $|\psi_c(\mathbf{r})|^2$ (a) and $\vec{\nabla}V(\mathbf{r})$ (b) as a function of distance z along the c -axis of BiTeI, obtained via semilocal (PBE) and dispersion-corrected (PBE-D2) calculations. The location of the unary Bi, Te, and I layers are marked by the vertical dashed lines.

SOC) to 1.246 eV (PBE-D2 w/o SOC) owing to the dispersion correction, which is further reduced to 0.207 eV (PBE-D2) via inclusion of SOC. Thus, the reduction in the value of E_g is largely due to SOC (rather than the dispersion correction). Accordingly, strong (weak) SOC implies a smaller (larger) band gap, which corresponds to a greater (smaller) value of the Rashba parameter. Hence E_g and α_R are roughly inversely proportional to each other, which is also noted in a recent study⁵⁰ on the $(\text{BiTeI})_m(\text{Bi}_2\text{Te}_3)_n$ heterostructures.

- * sumeyra@gtu.edu.tr
† cetin_kilic@gtu.edu.tr
- ¹ K. Ishizaka, M. S. Bahramy, H. Murakawa, M. Sakano, T. Shimojima, T. Sonobe, K. Koizumi, S. Shin, H. Miyahara, A. Kimura, K. Miyamoto, T. Okuda, H. Namatame, M. Taniguchi, R. Arita, N. Nagaosa, K. Kobayashi, Y. Murakami, R. Kumai, Y. Kaneko, Y. Onose, and Y. Tokura, *Nat. Mater.* **10**, 521 (2011).
 - ² M. S. Bahramy, B. J. Yang, R. Arita, and N. Nagaosa, *Nat. Commun.* **3**, 679 (2012).
 - ³ X. Xi, C. Ma, Z. Liu, Z. Chen, W. Ku, H. Berger, C. Martin, D. B. Tanner, and G. L. Carr, *Phys. Rev. Lett.* **111**, 155701 (2013).
 - ⁴ M. K. Tran, J. Levallois, P. Lerch, J. Teyssier, A. B. Kuzmenko, G. Autès, O. V. Yazyev, A. Ubaldini, E. Giannini, D. van der Marel, and A. Akrap, *Phys. Rev. Lett.* **112**, 047402 (2014).
 - ⁵ M. S. Bahramy, R. Arita, and N. Nagaosa, *Phys. Rev. B* **84**, 041202 (2011).
 - ⁶ S. V. Eremeev, I. A. Nechaev, Y. M. Koroteev, P. M. Echenique, and E. V. Chulkov, *Phys. Rev. Lett.* **108**, 246802 (2012).
 - ⁷ V. A. Kulbachinskii, V. G. Kytin, A. A. Kudryashov, A. N. Kuznetsov, and A. V. Shevelkov, *J. Solid State Chem.* **193**, 154 (2012).
 - ⁸ I. Y. Sklyadneva, R. Heid, K.-P. Bohnen, V. Chis, V. A. Volodin, K. A. Kokh, O. E. Tereshchenko, P. M. Echenique, and E. V. Chulkov, *Phys. Rev. B* **86**, 094302 (2012).
 - ⁹ H. Fu, *Phys. Rev. B* **87**, 075139 (2013).
 - ¹⁰ I. P. Rusinov, I. A. Nechaev, S. V. Eremeev, C. Friedrich, S. Blügel, and E. V. Chulkov, *Phys. Rev. B* **87**, 205103 (2013).
 - ¹¹ Z. Zhu, Y. Cheng, and U. Schwingenschlögl, *New J. Phys.* **15**, 023010 (2013).
 - ¹² M. Kanou and T. Sasagawa, *J. Physics: Condensed Matter* **25**, 135801 (2013).
 - ¹³ C.-R. Wang, J.-C. Tung, R. Sankar, C.-T. Hsieh, Y.-Y. Chien, G.-Y. Guo, F. C. Chou, and W.-L. Lee, *Phys. Rev. B* **88**, 081104 (2013).
 - ¹⁴ Y. Chen, X. Xi, W.-L. Yim, F. Peng, Y. Wang, H. Wang, Y. Ma, G. Liu, C. Sun, C. Ma, Z. Chen, and H. Berger, *J. Phys. Chem. C* **117**, 25677 (2013).
 - ¹⁵ A. Shevelkov, E. Dikarev, R. Shpanchenko, and B. Popovkin, *J. Solid State Chem.* **114**, 379 (1995).
 - ¹⁶ S. Grimme, *J. Comp. Chem.* **27**, 1787 (2006).
 - ¹⁷ A. Rabenau, H. Rau, and G. Rosenstein, *J. Less Common Metals* **21**, 395 (1970).
 - ¹⁸ J. Fenner and D. Mootz, *J. Solid State Chem.* **24**, 367 (1978).
 - ¹⁹ D.-K. Seo, M.-H. Whangbo, K. Neiningner, and G. Thiele, *J. Solid State Chem.* **137**, 206 (1998).
 - ²⁰ J. P. Perdew, K. Burke, and M. Ernzerhof, *Phys. Rev. Lett.* **77**, 3865 (1996).
 - ²¹ M. Amft, S. Lebègue, O. Eriksson, and N. V. Skorodumova, *J. Phys.: Condensed Matter* **23**, 395001 (2011).
 - ²² A. T. Clay, C. M. Kuntz, K. E. Johnson, and A. L. L. East, *J. Chem. Phys.* **136**, 124504 (2012).
 - ²³ P. E. Blöchl, *Phys. Rev. B* **50**, 17953 (1994).
 - ²⁴ G. Kresse and D. Joubert, *Phys. Rev. B* **59**, 1758 (1999).
 - ²⁵ G. Kresse and J. Furthmüller, *Phys. Rev. B* **54**, 11169 (1996).
 - ²⁶ D. Hobbs, G. Kresse, and J. Hafner, *Phys. Rev. B* **62**, 11556 (2000).
 - ²⁷ M. Marsman and J. Hafner, *Phys. Rev. B* **66**, 224409 (2002).
 - ²⁸ T. Bucko, J. Hafner, S. Lebegue, and J. G. Angyan, *J. Phys. Chem. A* **114**, 11814 (2010).
 - ²⁹ H. J. Monkhorst and J. D. Pack, *Phys. Rev. B* **13**, 5188 (1976).
 - ³⁰ R. J. Angel, edited by R. M. Hazen and R. T. Downs, *High-pressure and high-temperature crystal chemistry, Reviews in Mineralogy and Geochemistry, Vol. 41 (2000) Chap. 2*, pp. 35–59.
 - ³¹ A. Strachan, T. Çağın, and W. A. Goddard, *Phys. Rev. B* **60**, 15084 (1999).
 - ³² D. Lide, *CRC handbook of chemistry and physics : a ready-reference book of chemical and physical data* (CRC, Boca Raton, Fla. London, 2008).
 - ³³ One obtains $\chi_{\text{Te}} - \chi_{\text{Au}} = -0.30$, $\chi_{\text{Te}} - \chi_{\text{Pd}} = -0.10$, $\chi_{\text{Te}} - \chi_{\text{Bi}} = 0.20$, $\chi_{\text{I}} - \chi_{\text{Au}} = 0.26$, $\chi_{\text{I}} - \chi_{\text{Pd}} = 0.46$, $\chi_{\text{I}} - \chi_{\text{Te}} = 0.56$, and $\chi_{\text{I}} - \chi_{\text{Bi}} = 0.76$, using the elemental electronegativities³² (on Pauling's scale).
 - ³⁴ See Supplemental Material for (i) Table S1 that contains the calculated and experimental bond lengths and bond angles in the MeTeI (Me=Bi, Au, Pd) crystals, (ii) Figure S1 that displays the BM fits with $k_{\text{max}} = 4$ for BiTeI and 3 for AuTeI and PdTeI, (iii) Figure S2 that shows a comparison of the calculated and experimental pressure-volume curves for BiTeI. (iv) Figure S3 that displays the *bc* planar average of the gradient of the BiTeI crystal potential as a function of distance *x* along the *a*-axis.
 - ³⁵ E. Tasci, G. de la Flor, D. Orobengoa, C. Capillas, J. Perez-Mato, and M. Aroyo, *EPJ Web of Conferences* **22**, 00009 (2012).
 - ³⁶ Z. Aliev and M. Babanly, *Inorganic Materials* **44**, 1076 (2008).
 - ³⁷ K. Kunc and K. Syassen, *Phys. Rev. B* **81**, 134102 (2010).
 - ³⁸ A. L. Goodwin, D. A. Keen, and M. G. Tucker, *PNAS (USA)* **105**, 18708 (2008).
 - ³⁹ A. D. Fortes, E. Suard, and K. S. Knight, *Science* **331**, 742 (2011).
 - ⁴⁰ W. Li, M. R. Probert, M. Kosa, T. D. Bennett, A. Thirumurugan, R. P. Burwood, M. Parinello, J. A. K. Howard, and A. K. Cheetham, *J. Am. Chem. Soc.* **134**, 11940 (2012).
 - ⁴¹ A. B. Cairns, J. Catafesta, C. Levelut, J. Rouquette, A. van der Lee, L. Peters, A. L. Thompson, V. Dmitriev, J. Haines, and A. L. Goodwin, *Nature Mat.* **12**, 212 (2013).
 - ⁴² M. Hanfland, H. Beister, and K. Syassen, *Phys. Rev. B* **39**, 12598 (1989).
 - ⁴³ T. Okuda and A. Kimura, *J. Phys. Soc. Jpn* **82**, 021002 (2013).
 - ⁴⁴ J. S. Lee, G. A. H. Schober, M. S. Bahramy, H. Murakawa, Y. Onose, R. Arita, N. Nagaosa, and Y. Tokura, *Phys. Rev. Lett.* **107**, 117401 (2011).
 - ⁴⁵ M. Sakano, J. Miyawaki, A. Chainani, Y. Takata, T. Sonobe, T. Shimojima, M. Oura, S. Shin, M. S. Bahramy, R. Arita, N. Nagaosa, H. Murakawa, Y. Kaneko, Y. Tokura, and K. Ishizaka, *Phys. Rev. B* **86**, 085204 (2012).

- ⁴⁶ T. Ideue, J. G. Checkelsky, M. S. Bahramy, H. Murakawa, Y. Kaneko, N. Nagaosa, and Y. Tokura, *Phys. Rev. B* **90**, 161107 (2014).
- ⁴⁷ D. VanGennep, S. Maiti, D. Graf, S. W. Tozer, C. Martin, H. Berger, D. L. Maslov, and J. J. Hamlin, *J. Phys.: Condensed Matter* **26**, 342202 (2014).
- ⁴⁸ K. Momma and F. Izumi, *J. Appl. Cryst.* **44**, 1272 (2011).
- ⁴⁹ V. Kulbachinskii, V. Kytin, Z. Lavrukhina, A. Kuznetsov, and A. Shevelkov, *Semiconductors* **44**, 1548 (2010).
- ⁵⁰ J.-J. Zhou, W. Feng, Y. Zhang, S. A. Yang, and Y. Yao, *Sci. Rep.* **4** (2014).

SUPPLEMENTAL MATERIAL

- Table S1 lists the calculated and experimental bond lengths and bond angles in the MeTeI (Me=Bi, Au, Pd) crystals.
- Figure S1 displays a plot of the energy difference ΔE versus the volume, and the BM fits with $k_{\max} = 4$ for BiTeI and $k_{\max} = 3$ for AuTeI and PdTeI.
- Figure S2 shows a comparison of the calculated and experimental pressure-volume curves for BiTeI.
- Figure S3 displays the bc planar average of the gradient of the BiTeI crystal potential as a function of distance x along the a -axis.

TABLE S1. The calculated (PBE and PBE-D2) and experimental bond lengths d (in Å) and bond angles θ (in °) of the MeTeI crystals. The experimental values are taken from Refs. 15, 18, and 19 for BiTeI, AuTeI, and PdTeI, respectively. The labeling of bond lengths and angles are therefore the same as in the latter references.

	PBE	PBE-D2	Experimental
BiTeI			
$d_{\text{Bi-Te}}$	3.08	3.04	3.27 ^a
$d_{\text{Bi-I}}$	3.31	3.30	3.04 ^a
$\theta_{\text{Te-Bi-Te}}$	92.03	89.55	83.05 ^b
$\theta_{\text{Te-Bi-I}}$	174.45	174.10	174.43 ^b
$\theta_{\text{Te-Bi-I}}$	91.82	94.63	92.79 ^b
$\theta_{\text{I-Bi-I}}$	84.06	80.90	91.11 ^b
AuTeI			
$d_{\text{Au-I}}$	2.719	2.711	2.680
$d_{\text{Au-Te}}$	2.671	2.665	2.642
$d_{\text{Au-Te(I)}}$	2.702	2.694	2.654
$d_{\text{Au-Te(II)}}$	2.727	2.694	2.684
$d_{\text{Te}\cdots\text{Te(I)}}$	3.337	3.375	3.235
$d_{\text{Au}\cdots\text{I(I)}}$	3.711	3.584	3.500
$d_{\text{Au}\cdots\text{I(II)}}$	3.753	3.791	3.633
$d_{\text{Au}\cdots\text{Au(I)}}$	4.212	4.163	4.193
$d_{\text{Au}\cdots\text{Au(II)}}$	4.143	4.034	4.000
$d_{\text{Au}\cdots\text{Au(III)}}$	3.998	3.700	3.843
$\theta_{\text{I-Au-Te}}$	160.89	158.97	160.26
$\theta_{\text{I-Au-Te(I)}}$	85.99	84.27	86.17
$\theta_{\text{I-Au-Te(II)}}$	100.78	100.79	100.09
$\theta_{\text{Te-Au-Te(I)}}$	76.77	78.07	75.29
$\theta_{\text{Te-Au-Te(II)}}$	98.02	98.44	99.40
$\theta_{\text{Te(I)-Au-Te(II)}}$	163.69	170.06	167.71
$\theta_{\text{Au-Te-Au(I)}}$	103.23	101.93	104.71
$\theta_{\text{Au-Te-Au(II)}}$	100.25	97.65	97.34
$\theta_{\text{Au(I)-Te-Au(II)}}$	94.86	86.75	92.12
PdTeI			
$d_{\text{Pd-Te}_{\parallel}}$	2.636	2.629	2.601
$d_{\text{Pd-Te}_{\perp}}$	2.881	2.832	2.844
$d_{\text{Pd-I}}$	2.762	2.742	2.715
$d_{\text{Pd}\cdots\text{Pd}}$	4.047	3.946	3.952
$d_{\text{Pd}\cdots\text{Pd}}$	4.048	3.910	3.873
$d_{\text{Te}_{\parallel}\cdots\text{Te}_{\parallel}}$	3.377	3.532	3.385
$d_{\text{Te}_{\parallel}\cdots\text{Te}_{\perp}}$	3.727	3.772	3.706
$d_{\text{I}\cdots\text{I}}$	3.758	3.844	3.809
$\theta_{\text{Te}_{\parallel}\text{-Pd-Te}_{\parallel}}$	79.7	84.4	81.2
$\theta_{\text{I-Pd-I}}$	85.74	89.02	89.06
$\theta_{\text{Te}_{\perp}\text{-Pd-Te}_{\perp}}$	166.64	172.64	168.62

^aComputed by using the lattice parameters given in Tables 1 and 2 of Ref. 15 since in Ref. 15 the bond lengths given in Table 3 are *not* consistent with Tables 1 and 2, as noted by Bahramy *et al.* (Ref. 5).

^bNote that in Ref. 15 the bond angles given in Table 3 are consistent with Tables 1 and 2.

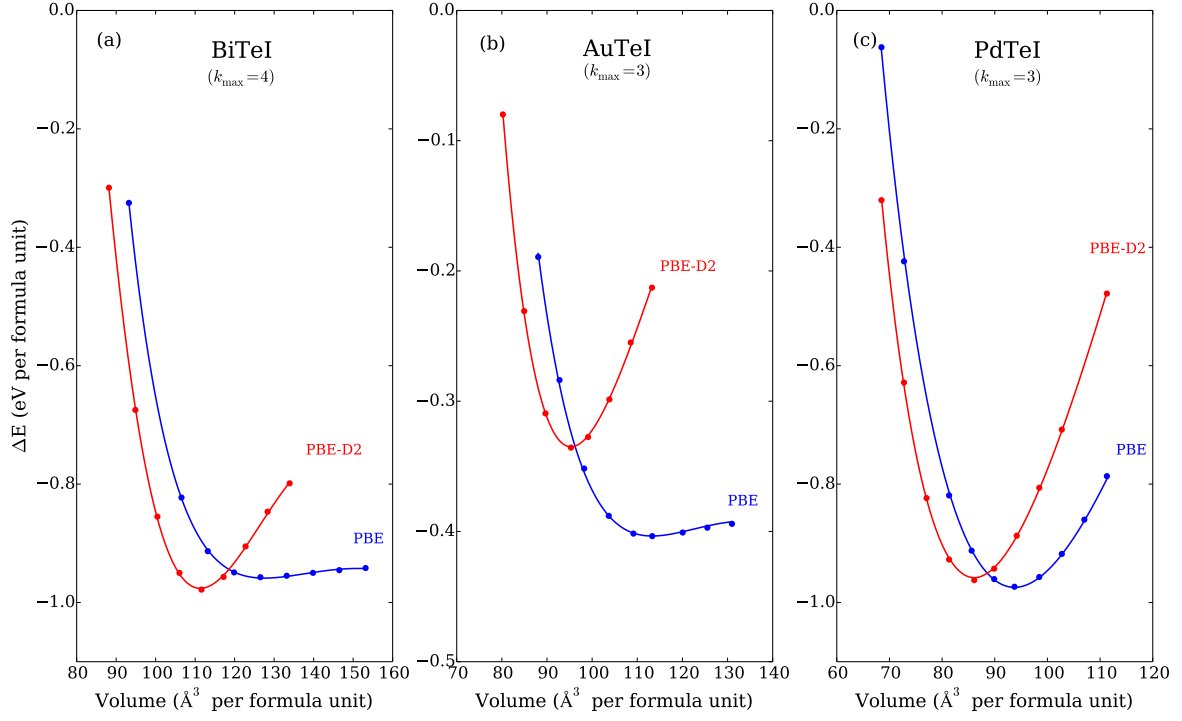


FIG. S1. (Color online) The plot of the energy difference $\Delta E = E - (E_{\text{Me}} + E_{\text{Te}} + E_{\text{I}})$, cf. Eq. (1), versus the volume for BiTeI (a), AuTeI (b), and PdTeI (c). Note that k_{\max} is reduced to 4 for BiTeI, and 3 for AuTeI and PdTeI. It is discernible that a good BM fit is achieved with these values of k_{\max} .

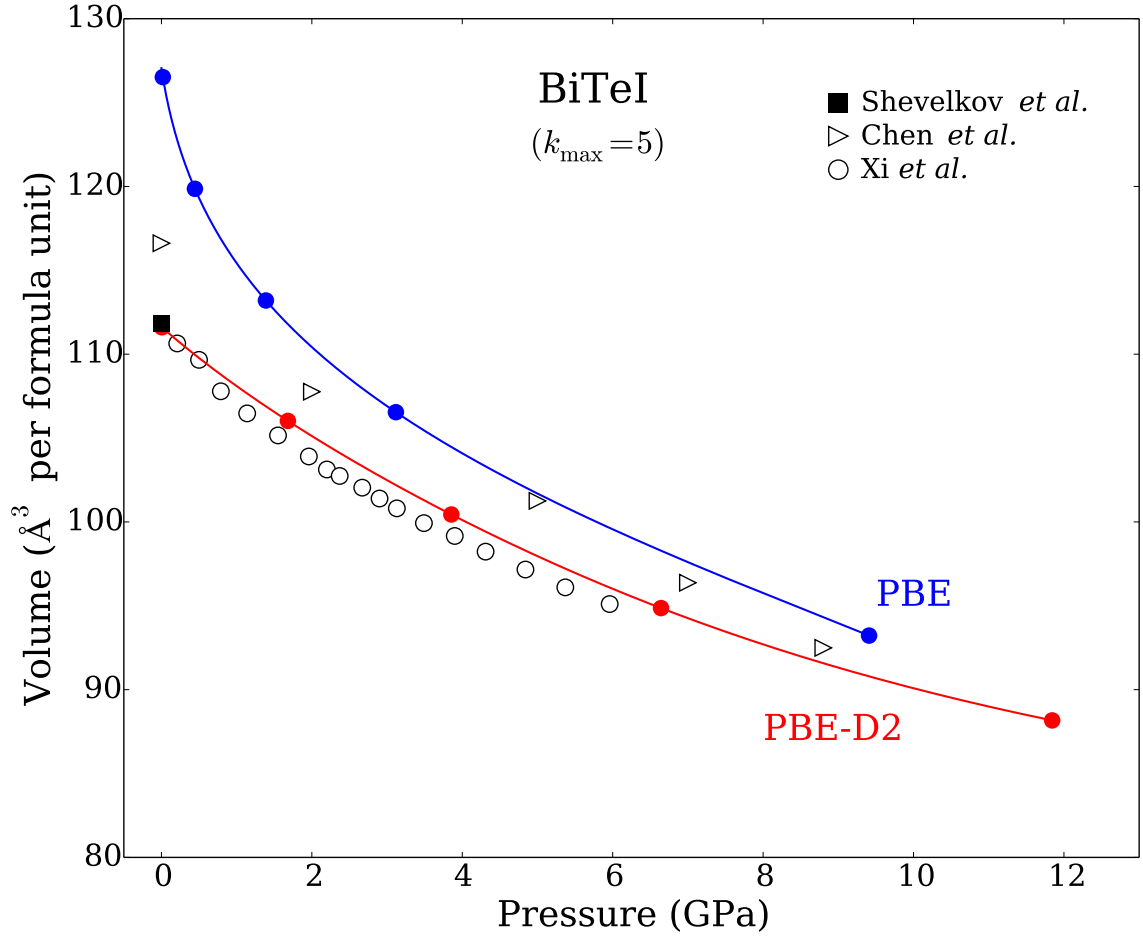


FIG. S2. (Color online) The calculated and experimental pressure-volume curves for BiTeI. The PBE-calculated and dispersion-corrected (PBE-D2) curves are in blue and red, respectively. The empty circles and triangles represent the experimental data provided by X. Xi (Ref. 3) and Y. Chen (Ref. 14), respectively. The filled square marks the experimental value of the equilibrium volume measured by Shevelkov *et al.* (Ref. 15).

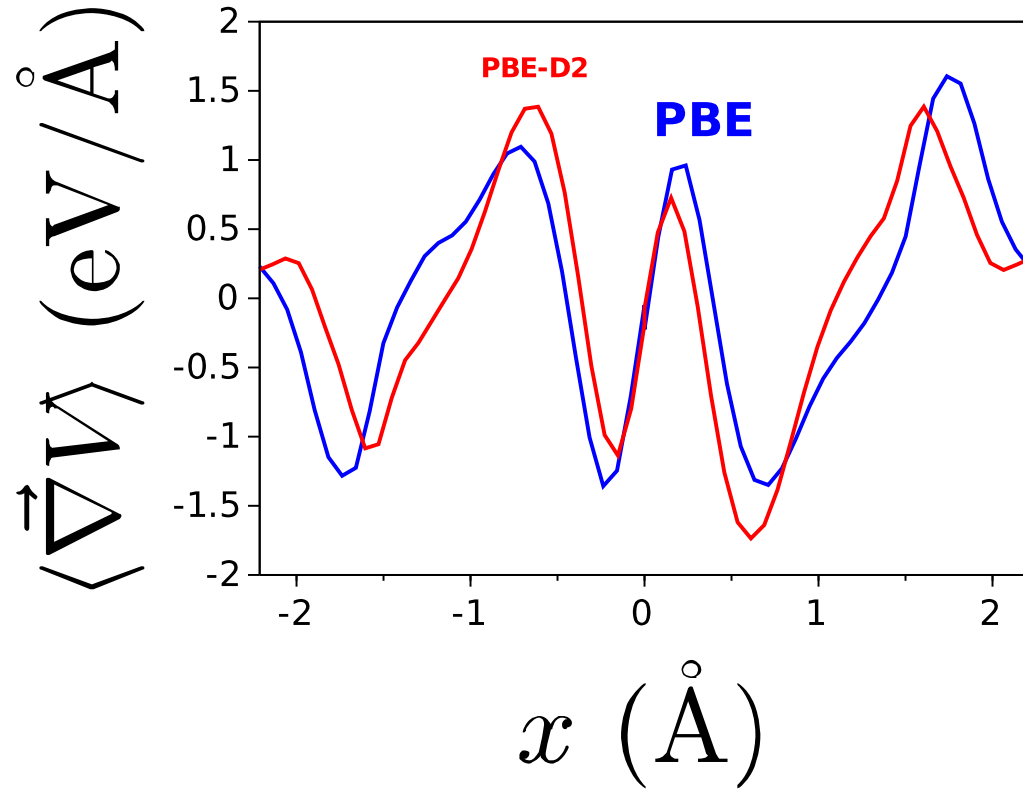


FIG. S3. (Color online) The bc planar average of the gradient of the BiTeI crystal potential as a function of distance x along the a -axis, obtained via semilocal (PBE) and dispersion-corrected (PBE-D2) calculations.